

Research Article

Open Access



Optimization of high-temperature energy storage properties of polyetherimide-based nanocomposite films via BST@CdS core-shell structure

Yuanhui Su¹ , Yu Huan¹ , Xue Wang¹, Jun Ouyang² , Tao Wei¹

¹School of Material Science and Engineering, University of Jinan, Jinan 250022, Shandong, China.

²Institute of Advanced Energy Materials and Chemistry, Jinan Engineering Laboratory for Multi-Scale Functional Materials, School of Chemistry and Chemical Engineering, Qilu University of Technology (Shandong Academy of Sciences), Jinan 250353, Shandong, China.

Correspondence to: Prof./Dr. Yu Huan, School of Material Science and Engineering, University of Jinan, 336 Nanxinzhuang West Road, Jinan 250022, Shandong, China. E-mail: mse_huany@ujn.edu.cn; Prof./Dr. Jun Ouyang, Institute of Advanced Energy Materials and Chemistry, Jinan Engineering Laboratory for Multi-Scale Functional Materials, School of Chemistry and Chemical Engineering, Qilu University of Technology (Shandong Academy of Sciences), 3501 Daxue Road, Jinan 250353, Shandong, China. E-mail: ouyangjun@qlu.edu.cn; Prof./Dr. Tao Wei, School of Material Science and Engineering, University of Jinan, 336 Nanxinzhuang West Road, Jinan 250022, Shandong, China. E-mail: mse_weit@ujn.edu.cn

How to cite this article: Su, Y.; Huan, Y.; Wang, X.; Ouyang, J.; Wei, T. Optimization of high-temperature energy storage properties of polyetherimide-based nanocomposite films via BST@CdS core-shell structure. *Microstructures* 2025, 5, 2025027. <https://dx.doi.org/10.20517/microstructures.2024.159>

Received: 13 Dec 2024 **First Decision:** 23 Jan 2025 **Revised:** 18 Feb 2025 **Accepted:** 25 Feb 2025 **Published:** 17 Mar 2025

Academic Editors: Dawei Wang, Jungho Ryu **Copy Editor:** Fangling Lan **Production Editor:** Fangling Lan

Abstract

Flexible dielectric composites stand as a promising candidate in high-power energy storage technology, but their practical application is hindered by low energy storage density (U_e), efficiency (η), and poor thermal stability at elevated temperatures. Herein, core-shell nanoparticles using barium strontium titanate coated with cadmium sulfide (BST@CdS) are designed and incorporated into polyetherimide (PEI) matrices as fillers to fabricate nanocomposite films. The CdS on the surface of BST nanoparticles, with its moderate dielectric constant, alleviates electric field mismatch between BST nanoparticles and PEI, while also introducing additional interfacial polarization. Additionally, the electron traps formed at the CdS/PEI interface can capture free and injected electrons. These features concurrently lead to an enhanced dielectric constant, reduced dielectric loss, and suppressed leakage current density, thereby boosting the energy storage performance of nanocomposite films. Accordingly, the optimized PEI/BST@CdS nanocomposite boasts an outstanding U_e of 9.4 J cm^{-3} and an η of 93.9% at 600 kV mm^{-1} and 25°C . Remarkably, even at 150°C , it still achieves superior energy storage performance with a



© The Author(s) 2025. **Open Access** This article is licensed under a Creative Commons Attribution 4.0 International License (<https://creativecommons.org/licenses/by/4.0/>), which permits unrestricted use, sharing, adaptation, distribution and reproduction in any medium or format, for any purpose, even commercially, as long as you give appropriate credit to the original author(s) and the source, provide a link to the Creative Commons license, and indicate if changes were made.



U_e of 4.4 J cm^{-3} and an η of 90.7% at 400 kV mm^{-1} . This study presents a viable approach for fabricating high-performance dielectric energy storage capacitors.

Keywords: Dielectric, energy storage, core-shell nanostructures, nanocomposite films, high temperature

INTRODUCTION

In recent years, dielectric capacitors, with high energy density (10^4 – 10^5 W kg^{-1}), long lifespan, and excellent stability, have exhibited widespread application potential in electronic and electric power components and systems^[1–6]. Polymer capacitors, compared to ceramic capacitors, offer superior breakdown strength (E_b)^[7–11]. Additionally, polymers possess intrinsic benefits such as flexibility, light weight, favorable reproducibility, cost-effectiveness, and the ability to be manufactured on a large scale.

Despite these advantages, the practical application of existing polymer capacitors is often curtailed by their modest operating temperatures. Biaxially oriented polypropylene (BOPP), as a typical material known for impressive E_b and energy storage efficiency (η)^[5,12], is extensively applied in the manufacturing of commercial polymer-based dielectric capacitors. Nevertheless, its utility becomes ineffective above 105°C , as rapidly increasing conduction losses severely degrade its electrical insulation and energy storage performance^[2,13,14]. This makes BOPP unsuitable for high-temperature applications, such as capacitors in inverters for hybrid and electric vehicles, where operational temperatures commonly exceed 140°C ^[15,16]. To meet these critical demands, substantial efforts have been directed toward the development of polymers exhibiting elevated glass transition temperatures (T_g). High-thermal-stability polymers, such as poly(ether ether ketone) (PEEK, with a T_g of around 150°C), polyetherimide (PEI, with a T_g of around 217°C), fluorene polyester (FPE, with a T_g of around 330°C), and polyimide (PI, with a T_g of around 360°C)^[17,18], are used as high-temperature polymer dielectrics^[19]. These polymers outperform BOPP in terms of thermal stability, and maintain exceptional electrical performance even under elevated temperature environments. Among these, PEI is selected as a matrix in this study due to its outstanding thermal stability and low level of dielectric loss ($\tan\delta$)^[20,21].

Although these high-thermal-stability polymers exhibit superior electrical properties compared to BOPP, their intrinsic low dielectric constant (ϵ_r) results in insufficient polarization intensity, thereby limiting the enhancement of discharge energy density (U_e)^[20,22–24]. Accordingly, a crucial requirement exists for effective design strategies to enhance the ϵ_r of these polymers. In response to this imperative, the researchers have introduced high- ϵ_r ceramic fillers into polymers, such as $\text{PbZr}_x\text{Ti}_{1-x}\text{O}_3$ ^[25,26], BaTiO_3 ^[20,27], $\text{BaSr}_x\text{Ti}_{1-x}\text{O}_3$ ^[28,29], and $\text{BaZr}_x\text{Ti}_{1-x}\text{O}_3$ ^[30]. These composites generally exhibit a significantly improved maximum electric displacement (D_{max}) and U_e compared to pure polymers. For example, Liu *et al.* demonstrated that combining $0.55\text{Bi}_{0.5}\text{Na}_{0.5}\text{TiO}_3$ – $0.45(\text{Bi}_{0.2}\text{Sr}_{0.7})\text{TiO}_3$ with PEI can achieve a high U_e of 10.37 J cm^{-3} , which represents a 1.65-fold increase over Pure PEI^[31].

To further enhance the energy storage performance of composite films, researchers have attempted to modify ceramic fillers with highly conductive materials such as silver, nickel, graphite, graphene, *etc.*^[29,32,33]. For instance, Jun *et al.* encapsulated BaTiO_3 particles with functionalized reduced graphene oxide flakes and mixed them with polymers to fabricate high- ϵ_r composites^[33]. Although this strategy significantly increases the ϵ_r near the percolation threshold, it also leads to increased $\tan\delta$ and decreased E_b , making it challenging to rely solely on enhancing the ϵ_r to improve U_e ^[29]. Furthermore, the significant difference of ϵ_r between inorganic nanofillers and organic matrix results in an uneven local electric field distribution at their interface, which would negatively impact the E_b of the composite materials^[34,35]. Meanwhile, the direct incorporation of ceramics with polymers often leads to a significant reduction in η , especially with rising

temperatures. For instance, Sun *et al.* prepared BaTiO₃/PI composites, achieving an η of 55.4% at 25 °C, but this decreased to 18.62% at 150 °C^[36]. This decrease was attributed to the large intrinsic remanent displacement (D_r) and poor thermal stability of BaTiO₃. Therefore, achieving effective dielectric compatibility between the incorporated filler and polymer matrix, while simultaneously optimizing the composite films for high D_{\max} and small D_r , remains a significant challenge for enhancing the high-temperature properties of polymer-ceramic composites.

Herein, using Ba_{0.7}Sr_{0.3}TiO₃ (BST) as the core material, which exhibits intrinsic high ϵ_r , high E_b and a slim hysteresis loop, we prepared core-shell structured BST@CdS nanoparticles by coating BST with CdS. These BST@CdS nanoparticles were subsequently incorporated into PEI to fabricate a series of nanocomposite films. The CdS shell layer with moderate ϵ_r serves to alleviate the electric field mismatch between BST nanoparticles and PEI matrix, while also introducing additional interfacial polarization. Additionally, the electron traps formed at the CdS/PEI interface can capture free and injected electrons. These features contribute to an enhanced ϵ_r , reduced $\tan\delta$, and suppressed leakage current density, thereby boosting the energy storage characteristics of PEI-based nanocomposite materials. Consequently, the optimized PEI/BST@CdS nanocomposite film exhibits an E_b of 600 kV mm⁻¹, an U_e of 9.4 J cm⁻³, and an η of 93.9% at 25 °C. Even at 150 °C, it maintains outstanding energy storage performance, with a U_e of 4.4 J cm⁻³ and an η of 90.7% at 400 kV mm⁻¹.

MATERIALS AND METHODS

Materials

PEI was acquired from PolyK. BaCl₂, SrCl₂·6H₂O, TiCl₄, NaOH, Cd(NO₃)₂·4H₂O, and Na₂S·9H₂O were sourced from Macklin. N-methyl-2-pyrrolidone (NMP) and 3-mercaptopropionic acid (MPA) were sourced from Sigma Aldrich. The chemicals employed in this study were utilized in their as-received state, without undergoing any additional purification processes.

Synthesis of Ba_{0.7}Sr_{0.3}TiO₃ (BST) nanoparticles

The synthesis of BST nanoparticles was conducted via a hydrothermal process. Firstly, a solution was prepared by mixing 0.437 g of BaCl₂, 0.24 g of SrCl₂·6H₂O, and 0.6 g of TiCl₄ in deionized water (35 mL), followed by stirring for half an hour at ambient temperature. Afterwards, 6 g of KOH was dissolved into the above solution, and stirred for an additional hour. The resulting mixture was then added into a 100-mL autoclave, and kept at 180 °C for 15 h. The white product was collected by centrifugal washing before drying at 60 °C overnight in air-drying to obtain white BST nanoparticles.

Synthesis of BST@CdS nanoparticles

First, 0.5 g of BST nanoparticles were added to deionized water, after which 20 μ L of functional agent MPA was introduced. The resulting mixture was magnetic stirred at ambient temperature for 4 h to completely functionalize the surface of the BST. Then, under heating and magnetic stirring at 90 °C, 0.054 g of Cd(NO₃)₂·4H₂O was added to the mixture. Subsequently, 2 mM Na₂S·9H₂O solution was gradually added to the mixture. The solution gradually turned yellow, indicating the formation of a CdS layer on the BST nanoparticles. The yellow precipitate was cleaned by centrifugation before drying at 60 °C overnight in an air-drying to obtain light yellow BST@CdS nanoparticles.

Preparation of PEI-based nanocomposite films

The preparation of PEI-based nanocomposite films containing BST@CdS nanoparticles is detailed below and visually represented in Figure 1. First, 1 g of PEI was dissolved into 8 g of NMP under magnetic stirring at 50 °C overnight. The required amounts of BST@CdS nanoparticle filler (1, 2, 3 wt%) were measured out and dispersed in 1 g of NMP solvent, followed by ultrasonic stirring at 300 W for 30 min to ensure uniform

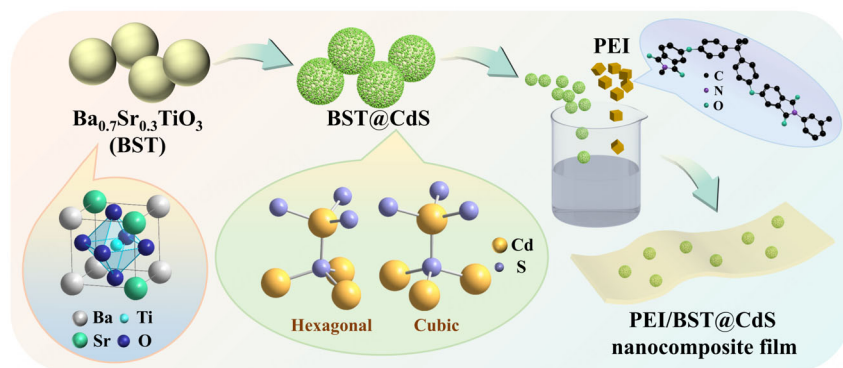


Figure 1. Preparation of PEI/BST@CdS nanocomposite films.

dispersion. The PEI/NMP solution and BST@CdS/NMP suspension were mixed and stirred for 24 h. Subsequently, this resulting mixture was cast onto a pristine glass substrate, and allowed to dry to form films. This initial drying phase took place at 80 °C for 6 h, and the secondary drying process took place at an elevated temperature of 200 °C for another 6-h interval. Following removal from the glass surface, the film was then subjected to a vacuum drying oven, where it was dried at 100 °C for 2 h to complete the dryness process. For clarity and ease of reference in subsequent discussions, the films were denoted as PEI/BST@CdS-1, PEI/BST@CdS-2, and PEI/BST@CdS-3, respectively. Additionally, for comparison, Pure PEI film consisting solely of pure PEI without any fillers, along with PEI/BST-2 nanocomposite film containing 2 wt% BST nanoparticles, was fabricated following the same experimental procedure. The thickness of the films ranged from 9 to 12 μm .

Characterization

The crystalline structures of synthesized materials were elucidated by X-ray diffraction (XRD) analysis utilizing a Bruker D8 system. Transmission electron microscopy (TEM; model JEOL-2011Plus, JEOL Ltd.) and scanning electron microscopy (SEM; Gemini300, Zeiss) were employed to analyze surface morphologies of the prepared nanoparticles. Surface morphologies of films were also examined by SEM. High-resolution TEM (HR-TEM), selected area electron diffraction (SAED), and energy dispersive X-ray spectroscopy (EDS) analyses were used to characterize the BST@CdS nanoparticles. X-ray photoelectron spectroscopy (XPS) measurements were conducted on an XPS instrument (ESCALAB QXi, Thermo Scientific). Electronic band structures of CdS and PEI were investigated using ultraviolet-visible diffuse reflectance spectroscopy (UV-Vis/DRS) spectra (UV-2600i, Shimadzu) and ultraviolet photoelectron spectroscopy (UPS, ESCALAB QXi, Thermo Scientific). Transmittance and color values of films were recorded using a benchtop spectrophotometer (CS-820, CHNSpec Technology). Transmittance spectra of films were measured between wavelengths of 370 and 780 nm. To ensure accuracy, each color value of the sample was tested 10 times, and the average value was calculated. Differential scanning calorimetry (DSC) curves of films were characterized with a Shimadzu analyzer (DSC-60). For electrical measurements, gold electrodes with diameters of 3 or 8 mm were applied to the films. ϵ_r and $\tan\delta$ were conducted over a frequency ranging from 10^3 to 10^6 Hz at 25 °C, employing an Agilent 4990A impedance analyzer. Temperature-dependent dielectric properties were measured from ambient temperature to 150 °C at 1 kHz (Agilent 4980A, Agilent). Electric displacement-electric field (D - E) hysteresis loops, E_b , and leakage current density of films were evaluated at 10 Hz with a ferroelectric analyzer (TF2000E, aixACCT).

RESULTS AND DISCUSSION

Structural analysis

To obtain BST@CdS nanoparticles, BST nanoparticles were first fabricated via a hydrothermal method, followed by the growth of a CdS shell using a chemical precipitation process. The SEM and TEM morphologies of BST nanoparticles are presented in [Figure 2A](#) and [B](#), while the corresponding images for BST@CdS nanoparticles are shown in [Figure 2C](#) and [D](#). These images reveal that the BST nanoparticles are smooth spherical with an average diameter of approximately 100 nm, while BST@CdS nanoparticles exhibit a large number of nanoscale nanoparticles around the spherical BST nanoparticles. Then, the phase structure of nanoparticles was investigated. XRD patterns, as depicted in [Figure 2E](#), reveal that the main diffraction peaks at 22.2° , 31.5° , 39.0° , 45.2° , 51.0° , 56.2° , and 65.7° correspond to the (100), (110), (111), (200), (210), (211), and (220) planes of the BST nanoparticles (JCPDS No. 89-0274), respectively. For BST@CdS nanoparticles, the diffraction peaks at 24.9° and 28.2° can be indexed to the planes of (100) and (002) of hexagonal CdS (marked with yellow asterisks). Another peak observed at 26.5° is ascribed to the lattice planes of (101) of the cubic CdS (marked with green asterisks). Furthermore, the HR-TEM image presented in [Figure 2F](#) reveals lattice fringes measuring 0.281 nm, which are assigned to the (101) plane of BST nanoparticles. Additionally, lattice fringes measuring 0.339 nm are observed, which correlate with the (111) planes of cubic CdS, and those with spacings of 0.363 and 0.245 nm are associated with the (100) and (102) of hexagonal CdS. [Figure 2G](#) displays the SAED pattern of BST@CdS nanoparticles, where rings correspond to the (101), (111) lattice planes of BST, the (331), (400) planes of cubic CdS, and the (200), (202) planes of hexagonal CdS, respectively.

The elemental distribution of the BST@CdS nanoparticle is characterized by EDS analysis [[Figure 2H](#)]. Ba, Sr, Ti, and O elements mostly concentrate in the center of particle, while Cd and S elements are localized at the periphery of spherical particle, forming a clear core-shell structure. Meanwhile, XPS spectra further confirm the presence of Cd and S in BST@CdS nanoparticles [[Figure 2I](#) and [J](#)]. Specifically, the binding energies at 411.3 and 404.5 eV are attributed to the Cd $3d_{3/2}$ and Cd $3d_{5/2}$ of Cd^{2+} , respectively, while peaks located at 161.6 and 162.7 eV can be ascribed to S $2p_{1/2}$ and S $2p_{3/2}$ in S^{2-} . Notably, slight shifts in the binding energies of the XPS spectra for the Ba and Ti elements in the BST@CdS sample, compared to those in the BST sample, indicate strong interactions between the BST core and the CdS shell [[Figure 2K](#)]. Thus, all these results collectively confirm the successful preparation of core-shell structured BST@CdS nanoparticles.

The energy band structures of PEI and CdS were investigated using UV-Vis/DRS and UPS spectra [[Figure 3A](#) and [B](#)]. According to Tauc's formula, the band gaps (E_g) of PEI and CdS are calculated using [Supplementary Equation 1](#), resulting in values of 3.2 eV for PEI and 2.3 eV for CdS. According to UPS measurement, the electron cutoff energy (E_{cutoff}) values of PEI and CdS are 16.32 and 15.65 eV, respectively, while their energy of the highest occupied molecular orbital (E_{homo}) values are 1.2 and 0.88 eV, respectively. Accordingly, the HOMO levels for PEI and CdS are determined to be -6.08 and -6.43 eV. Furthermore, lowest unoccupied molecular orbital (LUMO) levels are deduced by combining the E_g from the HOMO levels, determined to be -2.88 eV for PEI and -4.13 eV for CdS.

The schematic representation of the band structure for PEI and CdS is sketched in [Figure 3C](#), while the band structure diagrams on the interfaces of Electrode-PEI-CdS are sketched in [Figure 3D](#). Significantly, CdS has a lower LUMO energy level (-4.13 eV), in comparison to PEI (-2.88 eV), indicating its higher electron affinity. This characteristic enables it to effectively capture both the injected and excited electrons. Consequently, a significant trap level ($\Phi = E_{AC} - E_{AP}$) of 1.25 eV can be constructed [[Figure 3D](#)], facilitating the entrapment of electrons escaping from these trap sites^[37,38]. Notably, in the harsh environment

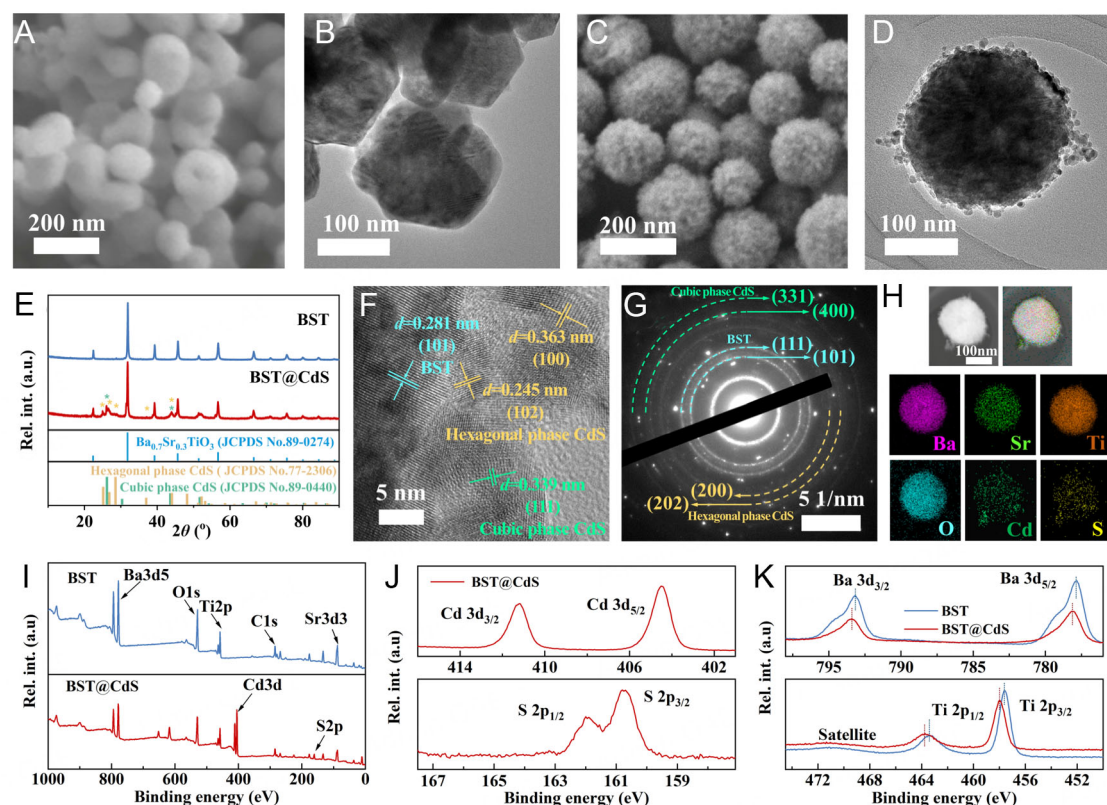


Figure 2. (A) SEM and (B) TEM morphologies of BST nanoparticles. (C) SEM and (D) TEM morphologies of BST@CdS nanoparticles. (E) XRD patterns of BST nanoparticles and BST@CdS nanoparticles. (F) HR-TEM image, (G) SAED patterns, and (H) EDS images of BST@CdS nanoparticle. (I) Survey spectra of BST and BST@CdS nanoparticles. High-resolution XPS spectra of BST and BST@CdS nanoparticles: (J) Cd 3d, S 2p, (K) Ba 3d, and Ti 2p.

characterized by elevated temperature and intensified electric fields, the presence of internal deeper traps introduced by the CdS in nanocomposite films would capture free electrons in the polymer and influence charge carrier injection and transport phenomena, which helps to reduce the energy loss. This mechanism justifies the exceptional energy storage performance characteristics observed in the nanocomposite films^[21,25,39].

A series of characterizations were carried out on the nanocomposite films. [Figure 4A](#) shows the surface morphology of Pure PEI, PEI/BST@CdS, and PEI/BST nanocomposite films. For Pure PEI film, a smooth surface is observed. In contrast, PEI/BST@CdS and PEI/BST nanocomposite films feature a uniform distribution of nanoparticles within PEI matrix, contributing to the improvement of E_b . Insets within [Figure 4A](#) provide a respective view of the cross-sectional morphology of the corresponding films. No significant internal defects or holes are observed in any films, suggesting their structural reliability. Transmittance of nanocomposite, serving as a key quality indicator, is investigated and depicted in [Figure 4B](#). It is found that Pure PEI exhibits the highest transmittance. With an enhancement in the content of BST@CdS, there is a slight reduction in the transmittance of PEI/BST@CdS nanocomposite films. Notably, at the same filler concentration, the PEI/BST-2 nanocomposite film exhibits a lower transmittance than PEI/BST@CdS-2, suggesting its poor compactness^[40,41]. Furthermore, to assess the uniformity of films, the color reproducibility of films was evaluated by measuring the color values at multiple randomly selected points and calculating the color difference (ΔE) using [Supplementary Equation 2](#)^[42-44], as depicted in [Figure 4C](#) and [Supplementary Figure 1](#). In comparison with Pure PEI films, the color of the PEI/BST@CdS

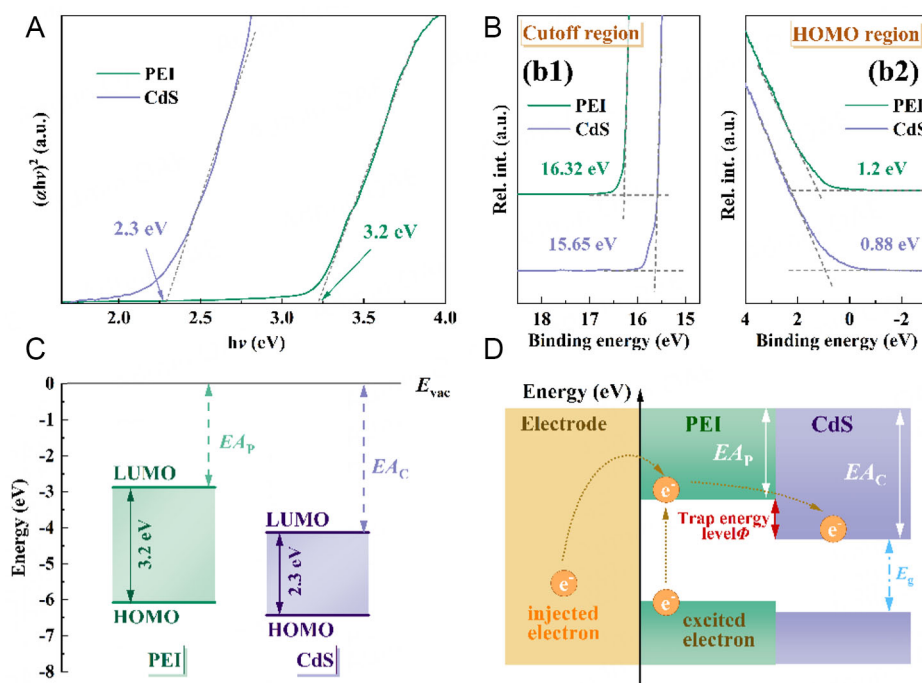


Figure 3. (A) Variation of $(\alpha h\nu)^2$ with photon energy ($h\nu$) of PEI and CdS. (B) UPS measurement of (b1) the cutoff region and (b2) the HOMO region for the PEI and CdS. (C) Schematic representation for band structure of PEI and CdS, with EA_p denoting the electron affinity of PEI and EA_c representing electron affinity of CdS. (D) The energy band diagrams on the interfaces of Electrode-PEI-CdS.

nanocomposite films gradually darkens due to the gradual increase in ceramic particle content, consistent with the optical images (see inset in Figure 4C). This color change can be visually measured by the ΔE calculated from the first test point of PEI as a standard sample, where the ΔE enhances with the content of filler particles. For each film, the ΔE values across multiple sites are very similar, indicating good color consistency and macroscopic uniformity, which contributes to excellent electrical performance reproducibility.

To delve deeper into the compositional analysis of the films, XRD tests were performed on Pure PEI, PEI/BST@CdS-2, and PEI/BST-2 nanocomposite film, as shown in Figure 4D. For all films, the broad peak around 22° is ascribed to PEI. For PEI/BST@CdS-2 and PEI/BST-2 nanocomposite films, a specific diffraction peak emerges at 31.5° , which is ascribed to the (110) plane of BST. For PEI/BST@CdS-2, a diffraction peak at 26.5° is observed, which is attributed to the cubic-phase CdS. Additionally, FTIR spectroscopy was employed to examine the film further^[45], with the resulting spectra presented in Figure 4E. The spectra reveal distinct absorption bands at 750 and $1,380\text{ cm}^{-1}$, attributed to C-N bending and stretching vibrations within the imidazole carbonyl functionalities of PEI, respectively. Characteristic absorption bands of asymmetric and symmetric carbonyl group stretching vibration were detected at $1,720$ and $1,780\text{ cm}^{-1}$, respectively. Additionally, a prominent peak measured at $1,209\text{ cm}^{-1}$ signifies the presence of C-O-C bonds. Other peaks at $1,478$, $1,504$, and $1,595\text{ cm}^{-1}$ denote bending vibrations characteristic of the benzene ring in PEI. Furthermore, Figure 4F shows DSC curves of films. Notably, both nanocomposite films, along with the Pure PEI film, have a T_g close to 220°C . This characteristic ensures the maintenance of their remarkable dielectric and energy storage characteristics even under elevated temperature conditions.

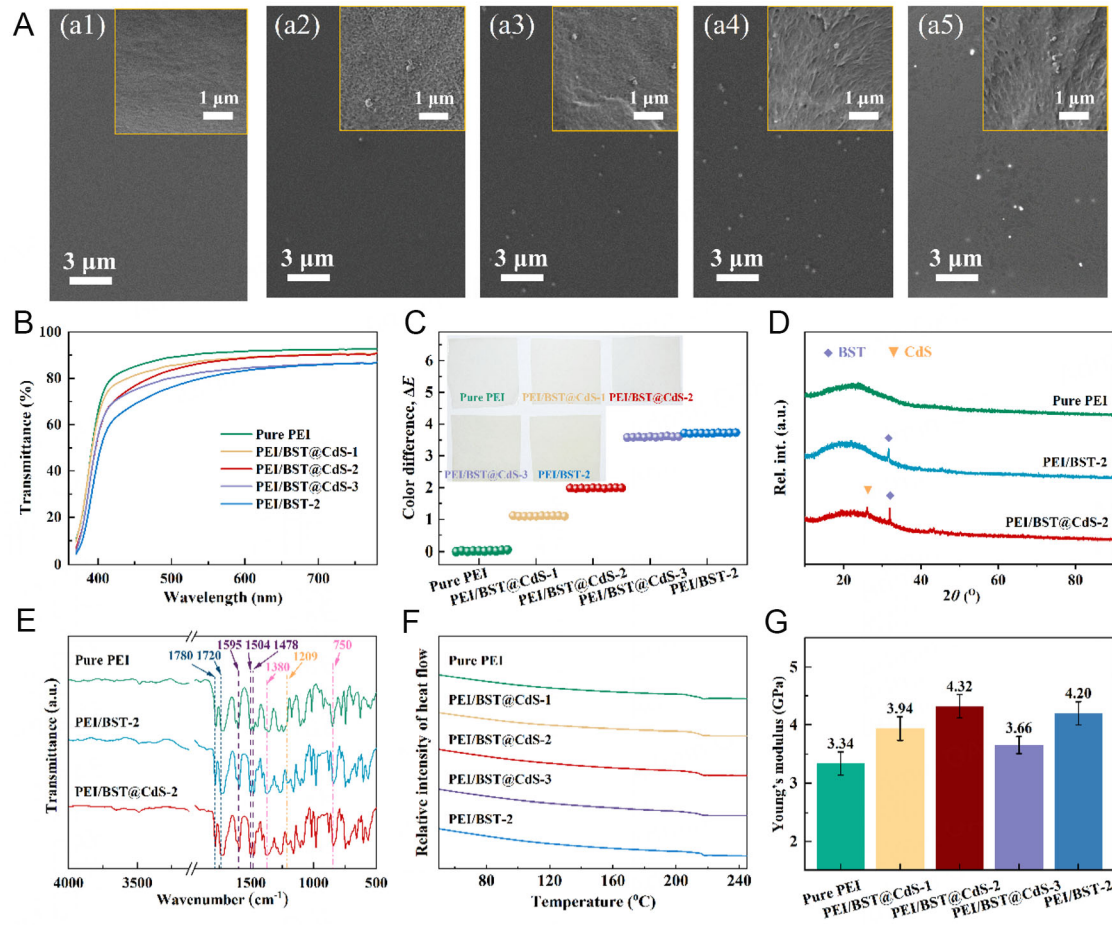


Figure 4. (A) Surface SEM images of nanocomposite films: (a1) Pure PEI, (a2) PEI/BST@CdS-1, (a3) PEI/BST@CdS-2, (a4) PEI/BST@CdS-3, and (a5) PEI/BST-2. Insets are the corresponding cross-section SEM images. (B) Transmittance spectra of nanocomposite films. (C) Color difference of nanocomposite films (Insets are optical photographs of films). (D) XRD patterns, (E) FTIR spectra, (F) DSC curves, and (G) Young's moduli of nanocomposite films.

The mechanical properties of films play a crucial role in determining their electrical E_b characteristics^[2,6,46–48]. Following the Stark-Garton model, the correlation between electrical E_b and Young's modulus can be defined through^[49]

$$E_b = 0.606 \sqrt{\frac{Y}{\epsilon_0 \epsilon_r}} \quad (1)$$

where Y represents Young's modulus, ϵ_0 indicates the dielectric constant of vacuum, and ϵ_r denotes the relative dielectric constant. This implies that an elevated Young's modulus fosters increased electrical E_b ^[2]. To this end, an investigation into Young's modulus of films was undertaken, as shown in Figure 4G. As the content of BST@CdS increases, Young's modulus of the nanocomposite films exhibits an upward trend before decreasing subsequently. The maximum of this trend is manifested in the PEI/BST@CdS-2 film, boasting Young's modulus of 4.32 GPa, marking a substantial 30% enhancement compared to the 3.34 GPa observed in Pure PEI. This improvement can be ascribed to the effective dispersity of BST@CdS nanoparticles, which facilitates stress distribution within the system^[35]. Such findings imply a heightened electrical breakdown for the PEI/BST@CdS-2 nanocomposite film. Conversely, a slight reduction in

Young's modulus for BST@CdS-3/PEI nanocomposite film is found, which is due to the excess filler content that leads to agglomeration of ceramic nanoparticles and severe branching of molecular chains within the nanocomposite film. This reduction in Young's modulus is detrimental to breakdown performance.

Dielectric properties of PEI/BST@CdS nanocomposite films

To delve into the dielectric characteristics of the films, both the ϵ_r and $\tan\delta$ of Pure PEI and nanocomposite films were measured across various frequencies, as illustrated in Figure 5A. The ϵ_r and $\tan\delta$ of films at 1 kHz were summarized in Supplementary Figure 2. As the frequency increases, the ϵ_r of PEI-based nanocomposite films slightly decreases, a phenomenon attributable to the suppression of interfacial polarization and dipole relaxation processes at elevated frequencies. Notably, the ϵ_r values of Pure PEI, PEI/BST@CdS-1, PEI/BST@CdS-2, PEI/BST@CdS-3, and PEI/BST-2 films are 3.3, 4.0, 4.6, 5.1, and 4.5, respectively. Given that ϵ_r of BST ($\epsilon_{r-BST} \approx 4,000$)^[29] is much higher than that of PEI ($\epsilon_{r-PEI} \approx 3.2$), the introduction of BST into the film leads to an increase in ϵ_r . Interestingly, PEI/BST@CdS-2 exhibits a higher ϵ_r than PEI/BST-2 although both have the same doping content. On the one hand, BST@CdS particles exhibit excess interfacial polarization due to charge transfer phenomena occurring at the core-shell interface, compared with the PEI/BST^[35,38,50,51]. On the other hand, the incorporation of CdS, which has a moderate ϵ_r ($\epsilon_{r-CdS} \approx 8.28$)^[52], on the surface of high- ϵ_r BST ceramic nanoparticles helps alleviate the electrical mismatch between BST particles and PEI matrices. Additionally, an increase in filler concentration (ranging from 1 to 3 wt%) within the PEI/BST@CdS nanocomposite films is accompanied by a rise in the ϵ_r , which is a consequence of enhanced polarization contribution, facilitating the energy storage performance. Figure 5B shows that all films exhibit low $\tan\delta$ over the examined frequency range. However, the $\tan\delta$ of PEI/BST-2 is higher than all the films, which is a consequence of the significant electric field distortion occurring at the interface between the PEI matrix and BST filler^[47,53]. Compared with PEI, with the BST@CdS filler concentration increasing, the tendency of $\tan\delta$ of PEI/BST@CdS initially decreases before increasing, reaching the lowest value in PEI/BST@CdS-2. This change can be explained by the fact that the introduction of the CdS layer can create profound trap energy states, which serve to effectively hinder charge carrier mobility and thereby suppress $\tan\delta$. However, excessive concentration of BST@CdS can cause microscopic defects, which in turn slightly elevates the $\tan\delta$.

In addition, the temperature-dependent dielectric properties of the films were studied, with Figure 5B illustrating the ϵ_r and $\tan\delta$ varying with temperature from 25 to 150 °C at 1 kHz. Both the ϵ_r and $\tan\delta$ remain stable within this temperature range, with little change as the temperature increases. This exceptional dielectric stability is ascribed to the elevated T_g of PEI, which is conducive to the desirable thermal stability of the nanocomposite films. With the testing temperature rising, a slight decline in ϵ_r of all films is observed. This phenomenon can be explained by the intensified thermal motion of dipoles, rendering their alignment along the applied electric field more challenging^[53]. Furthermore, at the same temperature, PEI/BST-2 film exhibits the highest $\tan\delta$, followed by Pure PEI, then PEI/BST@CdS-3, PEI/BST@CdS-1, and lastly PEI/BST@CdS-2, which is similar to the tendency at 25 °C. The incorporation of BST@CdS can significantly suppress the $\tan\delta$ of the films at elevated temperatures, a feature conducive to enhancing discharge energy storage efficiency.

Breakdown strength of PEI/BST@CdS nanocomposite films

The E_b is a crucial factor in influencing the energy storage properties of films. To evaluate this, Weibull distribution is employed, which can be determined using^[54-56]

$$P(E)=1-\exp\left[-\left(\frac{E}{E_b}\right)^\beta\right] \quad (2)$$

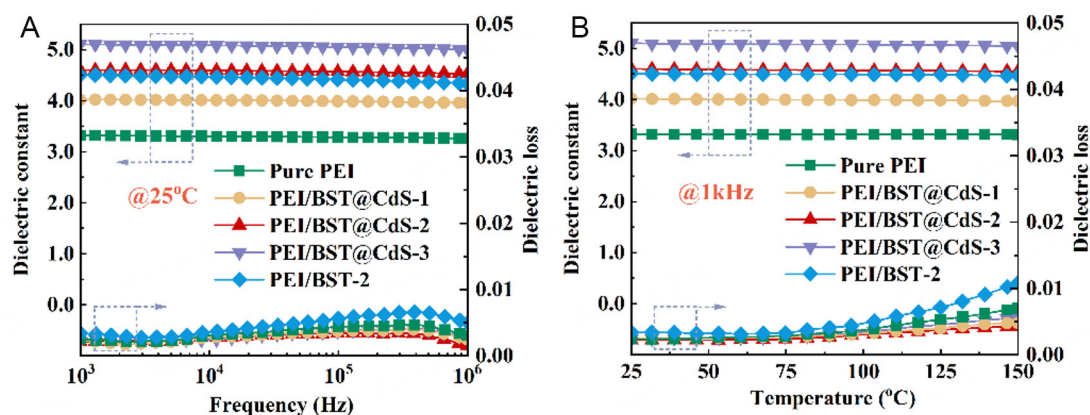


Figure 5. (A) Frequency dependence of dielectric constant (ϵ_r) and dielectric loss ($\tan\delta$) of nanocomposite films at 25 °C. (B) Temperature dependence of ϵ_r and $\tan\delta$ of nanocomposite films measured at 1 kHz.

Here, E denotes the specific breakdown electric field for each sample, while $P(E)$ represents the probability of electrical breakdown. E_b denotes a key parameter used to assess the electrical breakdown performance of films, representing the Weibull breakdown strength at $P(E) = 63.2\%$. Shape factor β signifies the concentration of the breakdown electric field and serves as a measure of test reliability and consistency. Figure 6A presents the Weibull breakdown strength of PEI-based films at 25 °C, while Supplementary Figure 3A compares the E_b and β of these films. All the nanocomposite films demonstrate a high β value, indicating their excellent uniformity and quality. Initially, as the loading content of BST@CdS rises, the E_b of nanocomposite films increases, followed by a subsequent decrease. A maximum E_b of 600 kV mm⁻¹ is obtained in PEI/BST@CdS-2 nanocomposite film. The moderate- ϵ_r CdS shell layer mitigates local electric field concentration between high- ϵ_r BST and low- ϵ_r PEI, alleviating uneven local electric fields. Concurrently, carriers in PEI/BST@CdS are captured by CdS/PEI internal deeper traps, significantly reducing leakage current density [Figure 6B]. Furthermore, the increased Young's modulus also contributes to the significant increase in E_b . However, excessive addition of BST@CdS may introduce defects in the PEI/BST@CdS-3 nanocomposite film, generating charge carriers and accelerating intrinsic breakdown, thereby reducing the E_b of the nanocomposite films.

Furthermore, Weibull breakdown strength of all films at 150 °C is summarized in Figure 6C, and a comparison of their E_b and β is depicted in Supplementary Figure 3B. The rise in temperature leads to a decrease in E_b for each sample due to the escape of electrons from trap centers and the generation of significant heat at high temperatures, leading to thermal accumulation and subsequent dielectric film degradation. Notably, PEI/BST@CdS-2 nanocomposite films still maintain an E_b of around 520 kV mm⁻¹ at 150 °C, demonstrating good high-temperature electrical insulation properties. In these films, moderate ϵ_r of the CdS shell layer effectively regulates the electric field distortion at the BST-PEI interface, thereby significantly reducing the local electric field strength. Remarkably, PEI/BST@CdS-2 maintains the lowest leakage current density across all temperatures because of the internal deeper traps [Figure 6D].

Energy storage properties of PEI/BST@CdS nanocomposite film

To further demonstrate the effectiveness and feasibility of incorporating BST@CdS nanoparticles in improving energy storage characteristics of nanocomposite films, their D - E hysteresis loops were recorded at 25 and 150 °C, at a testing frequency of 10 Hz [Supplementary Figures 4 and 5]. Figure 7A and B displays the representative D - E loops for films in proximity to their E_b at both 25 and 150 °C. As seen, as the electric field rises, the integral area of the closed D - E loop gradually widens, signifying a heightened energy loss

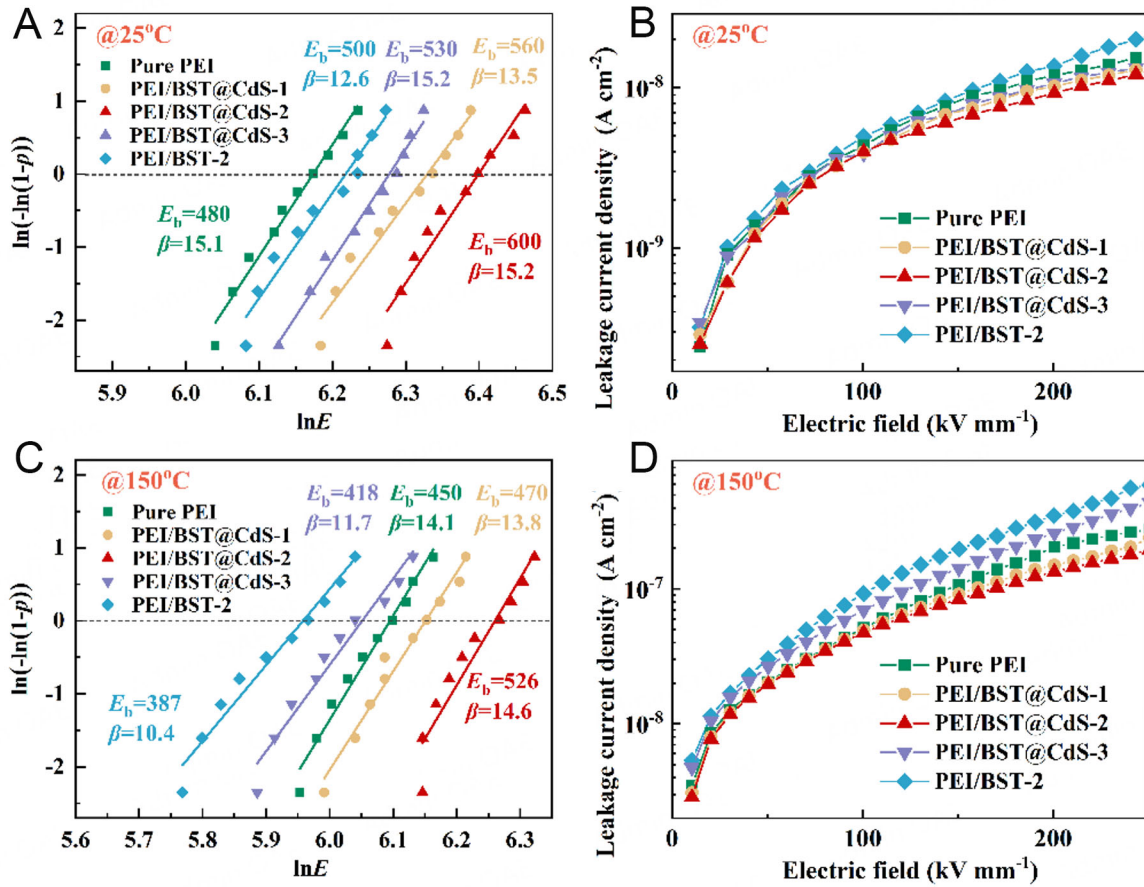


Figure 6. (A) Weibull breakdown strength, and (B) leakage current density of nanocomposite films at 25 °C. (C) Weibull breakdown strength, and (D) leakage current density of nanocomposite films at 150 °C.

associated with conduction processes. Particularly at 150 °C, energy loss becomes more severe. Notably, the D_{max} of all PEI/BST@CdS nanocomposite films exceeds that of Pure PEI films, which can be credited to the incorporation of BST@CdS fillers that enhance additional polarization response under external electric field application. However, as the BST@CdS content increases, the D_r also increases slightly, which is detrimental to maintaining good energy storage performance.

Accordingly, the energy storage performance, specifically the discharged energy storage density (U_e) and efficiency (η), was derived from the D - E loop data for the films [Supplementary Figures 4 and 5]. These parameters were calculated following the procedures given in

$$U_e = \int_{D_r}^{D_{max}} E dD \quad (3)$$

$$\eta = \frac{\int_{D_r}^{D_{max}} E dD}{\int_0^{D_{max}} E dD} \times 100\% \quad (4)$$

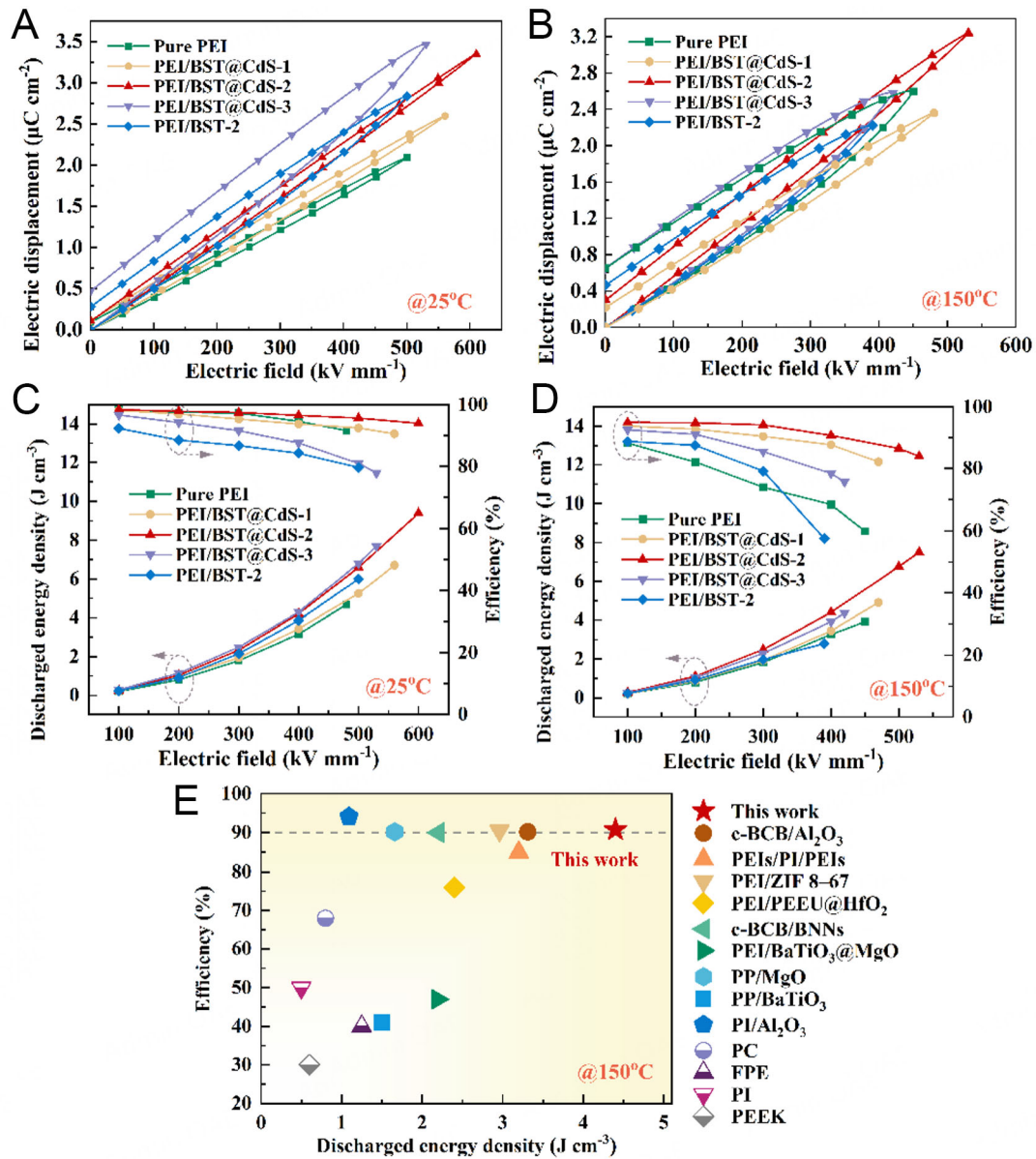


Figure 7. The unipolar D - E loops of films measured at (A) 25 °C and (B) 150 °C, respectively. (C) Energy storage properties of films measured at (C) 25 °C and (D) 150 °C, respectively. (E) Comparison of energy storage properties of PEI/BST@CdS-2 with recently reported high-temperature composites measured at 150 °C^[17,19,35,36,57-61].

where D signifies the electric displacement, E denotes the electric field, and D_r stands for remanent electric displacement. The results are visualized in Figure 7C and D, respectively^[55,56]. Obviously, the U_e value of PEI/BST@CdS and PEI/BST nanocomposite film exceeds that of Pure PEI film at an equivalent electric field, owing to the enhanced ϵ_r brought by the BST and BST@CdS fillers. Furthermore, the maximum energy storage properties of films are compared in Supplementary Figure 6A. Significantly, the U_e and η of PEI/BST@CdS-2 achieve 9.3 J cm^{-3} and 93.9% at 600 kV mm^{-1} , whereas those of PEI/BST-2 are only 5.9 J cm^{-3} and 79.5% at 500 kV mm^{-1} . On the one hand, the CdS shell layer in BST@CdS nanoparticles not only alleviates local electric field mismatch but also restricts the migration of charge carriers between the PEI and BST particles, resulting in an elevated E_b for PEI/BST@CdS films compared to PEI/BST films. On the other hand, BST@CdS nanoparticles exhibit a unique core-shell structure, which facilitates the introduction of

additional interfacial polarization within the nanocomposite film, contributing to extra electric displacement. Moreover, these enhancements can be further understood through the D - E loops of the films. Specifically, the D - E loop of PEI/BST@CdS-2 becomes thinner compared with PEI/BST-2 film, although they have the same nanoparticle weight fraction, which is closely related to the increasing D_{\max} and decreasing D_r . This observation is ascribed to the significant inhibition of $\tan\delta$ and leakage current density.

At 150 °C, all PEI films exhibit a further increase in D_r compared to their values measured at 25 °C. [Supplementary Figure 5 and Figure 7B]. The expansion of the D - E loops with rising temperature results from the heightened production and mobility of charge carriers at high temperatures, resulting in significant conduction losses and energy dissipation. Supplementary Figure 6B shows the comparison of maximum energy storage properties of films at 150 °C. Compared to Pure PEI films, the incorporation of BST@CdS nanoparticles significantly boosts both U_e and η values of films. PEI/BST@CdS-2 nanocomposite films demonstrate remarkable energy storage characteristics, achieving an impressive U_e of 7.5 J cm⁻³ and a moderate η of 84% at 530 kV mm⁻¹. These values are considerably greater than those observed for Pure PEI, which only attains a U_e of 3.9 J cm⁻³ and an η of 60% at 450 kV mm⁻¹ and 150 °C. However, as the content of BST@CdS nanoparticles further increases, the U_e and η values of PEI/BST@CdS-3 nanocomposite film decrease, which relates to the reduced E_b and prominent conduction losses at elevated temperatures. Moreover, the energy storage properties of nanocomposite films with $\eta > 90\%$ at 150 °C are summarized in Supplementary Figure 7. Specifically, PEI/BST@CdS-2 nanocomposite films maintain the highest U_e of 4.4 J cm⁻³. Compared to recently reported high-temperature polymer dielectric films, PEI/BST@CdS-2 dielectric nanocomposite films exhibit an excellent U_e [Figure 7E]^[17,19,35,36,57-61], demonstrating their potential value as dielectric nanocomposite films in high-temperature environments.

CONCLUSIONS

PEI/BST@CdS nanocomposites were prepared and systematically studied in this work. On the one hand, the CdS shell layer with moderate ε_r can alleviate the local electric field mismatch between the PEI polymer matrix and BST nanoparticles. The CdS shell layer with moderate ε_r can alleviate electric field mismatch between BST nanoparticles and PEI, while also introducing additional interfacial polarization. Meanwhile, the electron traps formed at the CdS/PEI interface can capture free and injected electrons. These features contribute to an enhanced ε_r , reduced $\tan\delta$, and suppressed leakage current density, all of which bolster the energy storage performance of the composites. Consequently, the optimized PEI/BST@CdS nanocomposite film achieves an exceptional U_e of 9.38 J cm⁻³ and an η of 93.9% at 600 kV mm⁻¹. Remarkably, even at elevated temperatures of 150 °C, it maintains outstanding energy storage performance with an $\eta > 90\%$, reaching a peak U_e of 4.4 J cm⁻³ under an electric field of 400 kV mm⁻¹. These findings offer valuable insight for improving the energy storage characteristics of flexible nanocomposites at high temperatures.

DECLARATIONS

Authors' contributions

Conceptualization, funding acquisition, supervision, project administration, writing - review & editing: Huan, Y.

Funding acquisition, supervision, project administration: Ouyang, J.

Supervision, project administration: Wei, T.

Methodology, investigation, data curation, visualization, writing - original draft: Su, Y.

Investigation, data curation, validation: Wang, X.

All authors contributed to the manuscript and were involved in the discussion.

Availability of data and materials

The raw data supporting the findings of this study are available within this Article and its [Supplementary Materials](#). Further data is available from the corresponding authors upon reasonable request.

Financial support and sponsorship

The work was supported by the Shandong Province Key Fundamental Research Program (Grant No. ZR2022ZD39), Taishan Scholars Program (Grant No. tsqn202312214), and Natural Science Foundation of Shandong Province (Grant No. ZR2024QE104).

Conflicts of interest

All authors declared that there are no conflicts of interest.

Ethical approval and consent to participate

Not applicable.

Consent for publication

Not applicable.

Copyright

© The Author(s) 2025.

REFERENCES

1. Yang, M.; Guo, M.; Xu, E.; et al. Polymer nanocomposite dielectrics for capacitive energy storage. *Nat. Nanotechnol.* **2024**, *19*, 588-603. [DOI](#)
2. Yang, M.; Ren, W.; Guo, M.; Shen, Y. High-energy-density and high efficiency polymer dielectrics for high temperature electrostatic energy storage: a review. *Small* **2022**, *18*, e2205247. [DOI](#)
3. Luo, H.; Zhou, X.; Ellingford, C.; et al. Interface design for high energy density polymer nanocomposites. *Chem. Soc. Rev.* **2019**, *48*, 4424-65. [DOI](#)
4. Thakur VK, Gupta RK. Recent progress on ferroelectric polymer-based nanocomposites for high energy density capacitors: synthesis, dielectric properties, and future aspects. *Chem. Rev.* **2016**, *116*, 4260-317. [DOI](#) [PubMed](#)
5. Chen, Q.; Shen, Y.; Zhang, S.; Zhang, Q. Polymer-based dielectrics with high energy storage density. *Annu. Rev. Mater. Res.* **2015**, *45*, 433-58. [DOI](#)
6. Dang, Z. M.; Yuan, J. K.; Yao, S. H.; Liao, R. J. Flexible nanodielectric materials with high permittivity for power energy storage. *Adv. Mater.* **2013**, *25*, 6334-65. [DOI](#) [PubMed](#)
7. Cheng, W.; Xiaojie, L. High energy storage properties of 0.94Bi_{0.5}Na_{0.5}TiO₃-0.06BaTiO₃ ceramics by incorporating Sr_{0.8}Bi_{0.17}0.1Ti_{0.8}Zr_{0.2}O_{2.95}. *Microstructures* **2023**, *3*, 2023023. [DOI](#)
8. Wang, C.; Hou, L.; Huan, Y. Study on the structure and properties of (1-x)KNNS-xBFANZ lead-free piezoelectric ceramics. *Adv. Ceram.* **2023**, *44*, 490-6. [DOI](#)
9. Yang, Y.; Dou, Z.; Zou, K.; et al. Regulating local electric field to optimize the energy storage performance of antiferroelectric ceramics via a composite strategy. *J. Adv. Ceram.* **2023**, *12*, 598-611. [DOI](#)
10. Luo, X.; Yan, Z.; Luo, H.; et al. Greatly improved piezoelectricity and thermal stability of (Na, Sm) Co-doped CaBi₂Nb₂O₉ ceramics. *Adv. Powder. Mater.* **2023**, *2*, 100116. [DOI](#)
11. Duan, J.; Wei, K.; Du, Q.; Ma, L.; Qi, H.; Li, H. High-entropy tungsten bronze ceramics for large capacitive energy storage with near-zero losses. *Adv. Funct. Mater.* **2024**, *34*, 2409446. [DOI](#)
12. Liu, X.; Cheng, M.; Zhang, Y.; Xing, Y.; Dang, Z.; Zha, J. High-temperature polymer dielectric films with excellent energy storage performance utilizing inorganic outerlayers. *Compos. Sci. Technol.* **2024**, *245*, 110305. [DOI](#)
13. Fan, X.; Ding, X.; Wang, P.; et al. Ultra-low loading fillers induced excellent capacitive performance in polymer-based multilayer nanocomposites under harsh environments. *Small* **2024**, *20*, e2405786. [DOI](#)
14. Yuan, Q.; Wang, Y.; Zhang, Z.; et al. Polymer-based nanocomposites with one-dimensional nanofillers for dielectric energy storage at high temperatures. *ACS. Appl. Polym. Mater.* **2024**, *6*, 10136-48. [DOI](#)
15. Chen, J.; Ren, F.; Yin, N.; Mao, J. Significant enhancement of high-temperature capacitive energy storage in dielectric films through surface self-assembly of BNNS coatings. *Chem. Eng. J.* **2024**, *479*, 147581. [DOI](#)
16. Wang, P.; Yao, L.; Pan, Z.; et al. Ultrahigh energy storage performance of layered polymer nanocomposites over a broad temperature

- range. *Adv. Mater.* **2021**, *33*, e2103338. DOI
17. Niu, Y.; Dong, J.; He, Y.; et al. Significantly enhancing the discharge efficiency of sandwich-structured polymer dielectrics at elevated temperature by building carrier blocking interface. *Nano. Energy.* **2022**, *97*, 107215. DOI
18. Zeng, J.; Yan, J.; Li, B.; Zhang, X. Improved breakdown strength and energy storage performances of PEI-based nanocomposite with core-shell structured PI@BaTiO₃ nanofillers. *Ceram. Int.* **2022**, *48*, 20526-33. DOI
19. Li, Q.; Chen, L.; Gadinski, M. R.; et al. Flexible high-temperature dielectric materials from polymer nanocomposites. *Nature* **2015**, *523*, 576-9. DOI
20. Wu, X.; Song, G.; Zhang, W.; et al. Atomic layer deposition fabricated core-shell nanostructures for enhanced polyetherimide composite dielectrics. *J. Mater. Chem. A.* **2022**, *10*, 13097-105. DOI
21. Li, X.; Luo, H.; Yang, C.; et al. Enhancing high-temperature energy storage performance of PEI-based dielectrics by incorporating ZIF-67 with a narrow bandgap. *ACS. Appl. Mater. Interfaces.* **2023**, *15*, 41828-38. DOI
22. Xu, W.; Yang, G.; Jin, L.; et al. High-k polymer nanocomposites filled with hyperbranched phthalocyanine-coated BaTiO₃ for high-temperature and elevated field applications. *ACS. Appl. Mater. Interfaces.* **2018**, *10*, 11233-41. DOI
23. Zuo, P.; Jiang, J.; Wang, R.; et al. Poly(ether imide) poly(ether imide) nanocomposites with BaTiO₃@TiO₂@SiO₂ or BaTiO₃@SiO₂@TiO₂ fillers improve energy storage capacity and dielectric thermal stability. *ACS. Appl. Nano. Mater.* **2023**, *6*, 18381-93. DOI
24. Wu, X.; Tan, D. Q. Enhanced energy density of polyetherimide using low content barium titanate nanofillers. *J. Phys. Conf. Ser.* **2023**, *2500*, 012008. DOI
25. Fan, Z.; Gao, S.; Chang, Y.; et al. Ultra-superior high-temperature energy storage properties in polymer nanocomposites via rational design of core-shell structured inorganic antiferroelectric fillers. *J. Mater. Chem. A.* **2023**, *11*, 7227-38. DOI
26. Guo, R.; Luo, H.; Liu, W.; et al. High energy density in PVDF nanocomposites using an optimized nanowire array. *Phys. Chem. Chem. Phys.* **2018**, *20*, 18031-7. DOI
27. Dang, Z.; Lin, Y.; Yuan, Q.; et al. Ultrahigh dielectric energy density and efficiency in PEI-based gradient layered polymer nanocomposite. *Adv. Funct. Mater.* **2024**, *34*, 2406148. DOI
28. Su, Y.; Huan, Y.; Peng, B.; Wang, X.; Wu, L.; Wei, T. Energy storage properties of flexible dielectric composites containing Ba_{0.4}Sr_{0.6}TiO₃/MnO₂ heterostructures. *Chem. Eng. J.* **2023**, *452*, 139316. DOI
29. Gao, F.; Zhang, K.; Guo, Y.; Xu, J.; Szafran, M. (Ba, Sr)TiO₃/polymer dielectric composites-progress and perspective. *Prog. Mater. Sci.* **2021**, *121*, 100813. DOI
30. Feng, Y.; Xue, J.; Zhang, T.; et al. Double-gradients design of polymer nanocomposites with high energy density. *Energy. Storage. Mater.* **2022**, *44*, 73-81. DOI
31. Liu, Y.; Luo, H.; Xiong, H.; et al. Enhanced high-temperature capacitive energy storage by 0.55Bi_{0.5}Na_{0.5}TiO₃-0.45(Bi_{0.2}Sr_{0.7})TiO₃ nanofibers in polyetherimide nanocomposites. *ACS. Appl. Polym. Mater.* **2023**, *5*, 7277-87. DOI
32. Wang, D.; Zhou, T.; Zha, J.; Zhao, J.; Shi, C.; Dang, Z. Functionalized graphene-BaTiO₃/ferroelectric polymer nanodielectric composites with high permittivity, low dielectric loss, and low percolation threshold. *J. Mater. Chem. A.* **2013**, *1*, 6162. DOI
33. Jun, S.; Jung, D.; Kim, J.; Yu, S. Dielectric characteristics of graphene-encapsulated barium titanate polymer composites. *Mater. Chem. Phys.* **2020**, *255*, 123533. DOI
34. Wang, P.; Zhou, D.; Guo, H.; et al. Ultrahigh enhancement rate of the energy density of flexible polymer nanocomposites using core-shell BaTiO₃@MgO structures as the filler. *J. Mater. Chem. A.* **2020**, *8*, 11124-32. DOI
35. Dong, X.; Wang, Y.; Wang, Y.; Yu, J.; Hu, Z. Polyetherimide-based composites containing novel BaTiO₃@MgO nanofibers for high-temperature film capacitors. *Colloid. Surface. A. Physicochem. Eng. Asp.* **2024**, *697*, 134425. DOI
36. Sun, W.; Lu, X.; Jiang, J.; et al. Dielectric and energy storage performances of polyimide/BaTiO₃ nanocomposites at elevated temperatures. *J. App. Phys.* **2017**, *121*, 244101. DOI
37. Yuan, C.; Zhou, Y.; Zhu, Y.; et al. Polymer/molecular semiconductor all-organic composites for high-temperature dielectric energy storage. *Nat. Commun.* **2020**, *11*, 3919. DOI PubMed PMC
38. Drakopoulos, S. X.; Wu, J.; Maguire, S. M.; et al. Polymer nanocomposites: interfacial properties and capacitive energy storage. *Prog. Polym. Sci.* **2024**, *156*, 101870. DOI
39. Lin, J.; Jiang, J.; Zhou, Y.; et al. Constructing deep traps to achieve excellent dielectric properties in crystal-based HfO₂/PEI nanocomposite films with ultralow filler loadings. *ACS. Appl. Mater. Interfaces.* **2024**, *16*, 11880-9. DOI
40. Kanamori, T.; Han, Y.; Nagao, D.; Kamezawa, N.; Ishii, H.; Konno, M. Luminescence enhancement of ZnO-poly(methylmethacrylate) nanocomposite films by incorporation of crystalline BaTiO₃ nanoparticles. *Mater. Sci. Eng. B.* **2016**, *211*, 173-7. DOI
41. Ren, X.; Jin, L.; Peng, Z.; et al. Regulation of energy density and efficiency in transparent ceramics by grain refinement. *Chem. Eng. J.* **2020**, *390*, 124566. DOI
42. Tilley, R. J. D. Colour and the optical properties of materials: an exploration of the relationship between light, the optical properties of materials and color. John Wiley & Sons, Ltd, 2011. DOI
43. Wübbeler, G.; Campos, A. J.; Elster, C. Evaluation of uncertainties for CIELAB color coordinates. *Color. Res. Appl.* **2017**, *42*, 564-70. DOI
44. Su, Y.; Huan, Y.; Liu, W.; et al. Color-coding real-time detection for the health of lithium-ion batteries. *Acta. Mater.* **2025**, *283*, 120562. DOI
45. Ren, W.; Pan, J.; Dan, Z.; et al. High-temperature electrical energy storage performances of dipolar glass polymer nanocomposites filled with trace ultrafine nanoparticles. *Chem. Eng. J.* **2021**, *420*, 127614. DOI

46. Zhang, C.; Tong, X.; Zhang, T.; et al. Constructing a dual gradient structure of energy level gradient and concentration gradient to significantly improve the high-temperature energy storage performance of all organic composite dielectrics. *Chem. Eng. J.* **2024**, *491*, 151634. [DOI](#)
47. Hu, D.; Luo, H.; Liu, Y.; et al. Enhanced high-temperature performance of PEI dielectrics via deep trap energy levels and physically crosslinked effects. *Chem. Eng. J.* **2024**, *498*, 155398. [DOI](#)
48. Chen, X.; Wei, Y.; Wang, F.; et al. Enhanced high-temperature capacitive performance of PEI dielectrics by an adjustable Al_2O_3 interlayer. *ACS. Appl. Polym. Mater.* **2024**, *6*, 12616-22. [DOI](#)
49. Stark, K. H.; Garton, C. G. Electric strength of irradiated polythene. *Nature* **1955**, *176*, 1225-6. [DOI](#)
50. Nie, L.; Lin, J.; Zhang, P.; Zuo, P.; Liu, X.; Zhuang, Q. Significantly enhanced high-temperature energy storage capacity for polyetherimide-based nanocomposites via energy level modulation and electrostatic crosslinking. *J. Power. Sources.* **2025**, *626*, 235698. [DOI](#)
51. Sun, S.; Fan, K.; Yang, J.; et al. Surface modification engineering on polymer materials toward multilevel insulation properties and subsequent dielectric energy storage. *Mater. Today.* **2024**, *80*, 758-823. [DOI](#)
52. Bhunia, R.; Ghosh, D.; Ghosh, B.; Hussain, S.; Bhar, R.; Pal, A. K. Some aspects of microstructural and dielectric properties of nanocrystalline CdS/poly(vinylidene fluoride) composite thin films. *Polym. Int.* **2015**, *64*, 924-34. [DOI](#)
53. Feng, Y.; Zhou, Y.; Zhang, T.; et al. Ultrahigh discharge efficiency and excellent energy density in oriented core-shell nanofiber-polyetherimide composites. *Energy. Storage. Mater.* **2020**, *25*, 180-92. [DOI](#)
54. Zhang, X.; Shen, Y.; Zhang, Q.; et al. Ultrahigh energy density of polymer nanocomposites containing $\text{BaTiO}_3/\text{TiO}_2$ nanofibers by atomic-scale interface engineering. *Adv. Mater.* **2015**, *27*, 819-24. [DOI](#)
55. Hu, H.; Zhang, F.; Luo, S.; Chang, W.; Yue, J.; Wang, C. Recent advances in rational design of polymer nanocomposite dielectrics for energy storage. *Nano. Energy.* **2020**, *74*, 104844. [DOI](#)
56. Samantaray, S.; Mallick, P.; Hung, I.; Moniruzzaman, M.; Satpathy, S. K.; Mohanty, D. Ceramic-ceramic nanocomposite materials for energy storage applications: a review. *J. Energy. Storage.* **2024**, *99*, 113330. [DOI](#)
57. Ai, D.; Li, H.; Zhou, Y.; et al. Tuning nanofillers in situ prepared polyimide nanocomposites for high-temperature capacitive energy storage. *Adv. Energy. Mater.* **2020**, *10*, 1903881. [DOI](#)
58. Zhou, Y.; Yuan, C.; Wang, S.; et al. Interface-modulated nanocomposites based on polypropylene for high-temperature energy storage. *Energy. Storage. Mater.* **2020**, *28*, 255-63. [DOI](#)
59. Li, H.; Ai, D.; Ren, L.; et al. Scalable polymer nanocomposites with record high-temperature capacitive performance enabled by rationally designed nanostructured inorganic fillers. *Adv. Mater.* **2019**, *31*, e1900875. [DOI](#)
60. Lin, J.; Wu, X.; Xia, Y.; et al. The poly(arylene ether urea) double interface layer formed in PEEU/ HfO_2 /PEI nanocomposites enables enhanced dielectric and energy storage performance. *Surf. Interfaces.* **2024**, *49*, 104462. [DOI](#)
61. Wang, F.; Cai, J.; Yang, C.; et al. Improved capacitive energy storage nanocomposites at high temperature utilizing ultralow loading of bimetallic MOF. *Small* **2023**, *19*, e2300510. [DOI](#)